

Nucleation and Growth of Calcium Phosphate from Physiological Solutions onto Self-Assembled Templates by a Solution-Formed Nucleus Mechanism

B. J. Tarasevich,^{*,†} C. C. Chusuei,[‡] and D. L. Allara[§]

Pacific Northwest National Laboratory, Richland, Washington 99352, Department of Chemistry, University of Missouri, Rolla, Missouri 65409-0010, and Department of Chemistry and the Materials Research Institute, Pennsylvania State University, University Park, Pennsylvania 16802

Received: November 12, 2002; In Final Form: May 19, 2003

The nucleation and growth mechanisms of calcium phosphate were investigated using supersaturated solutions similar to physiological conditions and model self-assembled monolayer substrates tailored to have functional groups that mimicked chemistries found in bone organic matrices. Deposition kinetics were studied using an in situ microbalance and showed a long induction period followed by a second region of extensive growth, both of which depended on the solution supersaturation. Solution studies revealed that the growth of calcium phosphate onto the surfaces after the induction period corresponded to nucleation and growth in solution. Nuclei formed in solution, started to grow, adsorbed onto the substrates, and then grew further to form apatite films composed of coalesced, oriented crystallites. The solution-formed critical nucleus mechanism is in contrast to heterogeneous nucleation and reveals an important mechanism for calcium phosphate growth onto surfaces.

Introduction

The controlled nucleation and growth of calcium phosphate is essential for the formation of bone, tooth, and other mammalian hard tissue structures.¹ Undesirable nucleation can also occur onto arteriosclerotic vessel walls and biomaterial implant surfaces such as bioprosthetic heart valves, resulting in implant failure.² In both cases the mechanisms of nucleation and growth are not known, but are believed to involve an organic matrix template.

In bone, calcium phosphate deposits within gap regions of the collagen I fibril matrix. Calcium phosphate nucleates directly onto collagen fibrils,³ onto noncollagenous proteins associated with the collagen surface,^{4,5} or within matrix phosphoprotein vesicles which are transported to the collagenous matrix within woven bone and cartilage.⁶ Noncollagenous glycoproteins isolated from mineralizing tissue include bone sialoprotein,^{7,8} osteonectin,⁹ osteopontin,¹⁰ and bone acidic glycoprotein-75.¹¹ Bone sialoprotein is most commonly suggested as a calcium phosphate nucleation protein because of its expression at a late stage of osteoblast maturation, its presence at the onset of mineralization, its high affinity for calcium, and its ability to nucleate apatite in assays. Bone sialoprotein contains polyglutamic acid residues at 61–78 and 136–151 as well as sulfate and phosphate groups in the oligosaccharide regions. It has been suggested that the charged functionality initiates calcium phosphate nucleation by causing calcium binding.¹² In blood vessels and cardiovascular implants, it is believed that blood proteins such as fibrinogen¹³ or lipids such as cholesterol¹⁴ adsorb onto surfaces and act as calcium phosphate nucleators.

There have been numerous previous studies of calcium phosphate growth in model in vitro systems. These studies, in general, involve the growth of calcium phosphate thin films from

relatively high supersaturation solutions similar to physiological solutions onto planar substrates^{15–22} and nucleation and growth kinetic studies from lower supersaturation solutions onto suspended particles and macromolecules using the constant composition method.^{23–26} In several of the in vitro studies, calcium phosphate deposition is believed to be initiated by heterogeneous nucleation, the formation of critical nuclei onto the substrate. Nucleation has been associated with titania surfaces that have high Lewis base surface tension parameters,²⁷ negatively charged surfaces such as silica,¹⁹ modified polymers,¹⁸ and charged macromolecules.^{25,28} It has been suggested that calcium binding onto negative sites promotes heterogeneous nucleation.^{21,25,26,29} Nucleation may be initiated by nonspecific electrostatic interactions between the charged surface and charged crystal lattice faces. Alternatively, specific epitaxial relationships between the calcium phosphate lattice and organic functional groups have been proposed to promote nucleation.^{30,31}

Our work involves the use of self-assembled monolayers (SAMs) as nucleation templates. Self-assembled surfaces composed of alkanethiols adsorbed onto gold surfaces make very good model systems for the study of various surface and interfacial phenomena such as wetting,³² adsorption, and electrochemistry.³³ By a combination of S atom binding to 3-fold hollows at the Au(111) and interchain van der Waals forces, alkanethiols assemble into overall hexagonally ordered structures with interchain distances of 4.97 Å. SAMs with a wide range of functional end groups can be formed.³⁴ Recently, self-assembled monolayers have been used as model nucleation templates for the in vitro growth of oxide and oxyhydroxide films^{35,36} and calcium carbonate biomaterials.^{37,38} Terminal functional groups were used to mimic chemistries found in the biological nucleation proteins. Although self-assembled templates are not as complex as nucleation proteins, their structure and functionality are well-known and can be carefully controlled.

The SAMs were interfaced with a quartz crystal microbalance (QCM) which can be used in solution³⁹ to probe interfacial phenomena such as thin film deposition,⁴⁰ interfacial chemistry

* To whom correspondence should be addressed. Fax: (509) 375-2186.

[†] Pacific Northwest National Laboratory.

[‡] University of Missouri.

[§] Pennsylvania State University.

and reactions, and adsorption.⁴¹ The microbalance technique detects changes in mass on the order of nanograms per cm² at the liquid/solid interface. The QCM is especially convenient for studies involving thiol SAMs because the electrodes are often gold. The QCM operates by application of an rf frequency to electrodes attached to an AT cut quartz crystal, which causes formation of an acoustic wave due to the converse piezoelectric effect. The oscillator circuit tracks the resonant frequency which corresponds to the formation of standing acoustic waves in the thickness shear vibrational mode. The addition of a rigid layer to the quartz surface increases the shear wave wavelength, which reduces the resonance frequency.

Here, we report studies of the nucleation and growth kinetics of calcium phosphate onto self-assembled nucleation templates. SAMs were formed with end groups that mimicked aspartic and glutamic acid residues found in nucleation proteins (COOH). Some studies were also done with CH₃- and OH-terminated SAMs. The kinetics of nucleation and growth were studied as a function of solution type, SAM functionality, and solution supersaturation using the in situ microbalance technique. The composition and structure of adsorbates in the early stages of deposition were studied using X-ray photoelectron spectroscopy (XPS) and a time-of-flight secondary ion mass spectrometry (TOF-SIMS) technique involving (CsI)Cs⁺ projectiles. The solutions were studied for evidence of solution precipitation. The phase, orientation, and morphology of deposits were examined using glancing angle X-ray diffraction (XRD), atomic force microscopy (AFM), and field emission microscopy (FEM). The solution, kinetic, and adsorbate studies reveal a deposition mechanism involving solution-formed crystallites, not heterogeneous nucleation. This mechanism may be important in the in vitro growth of calcium phosphate films and in vivo bone growth.

Experimental Procedures

Self-Assembled Monolayer Formation and Characterization. *Thiol Synthesis.* *N*-Hexadecanethiol (Aldrich, 92%) was purified by vacuum distillation. 16-Mercaptohexadecanoic acid and 16-mercaptohexadecanol were synthesized using methods similar to those used previously⁴² except that the attachment of the thiol group by displacement of bromine was done using thiourea instead of sodium methoxide and thiolacetic acid. Br-(CH₂)₁₅CH₂OH and Br-(CH₂)₁₅COOH (2 g) were refluxed for 3 h with 0.44 g of thiourea in degassed ethanol. A 6 mL sample of 0.95 M NaOH was added to the flask, and the resulting solution was refluxed for an additional 2 h. The solution was cooled, and the thiol layer was separated from the water/ethanol solution. The water layer was acidified with dilute sulfuric acid and extracted with ether. The thiol was added to the ether and filtered using Celite. The ether was extracted with water and aqueous NaHCO₃ and removed by rotoevaporation. The resulting white solids were recrystallized from hexane as 16-mercaptohexadecanoic acid (mp 65–66 °C; ¹H NMR (CDCl₃) δ 2.53 (q, 2H), 2.35 (t, 2H), 1.62 (m, 4H), and 1.28 (m)) and 16-mercaptohexadecanol (mp 50–51 °C; ¹H NMR (CDCl₃) δ 3.64 (t, 2H), 2.52 (q, 2H), 1.55 (m, 4H), and 1.2–1.4 (m)).

SAM Formation. QCM crystals with freshly deposited gold were placed into freshly prepared 1 mM thiol solutions in absolute ethanol for at least 48 h. Companion samples consisting of 1 cm² silicon wafers and 2 in. diameter fused silica disks were also prepared for XPS and FTIR examination. Samples were removed and cleaned by ultrasonication in ethanol. The surfaces of the COOH SAMs were washed in 0.01 M HCl and water.

XPS Characterization. SAMs were characterized using a Physical Electronics Quantum 2000 scanning ESCA instrument with a focused monochromatic Al Kα X-ray (1486.6 eV) source, a spherical section analyzer, and a 16-element multichannel detection system. The data were taken using a 100 W, 100 μm diameter beam that was incident normal and rastered over a 1.5 mm by 0.2 mm rectangle on the sample. All spectra were recorded at a 45° takeoff angle for the photoelectrons. For each core level spectrum scans were averaged over a typical collection time of 5 min. The resolution (Ag 3d_{5/2}) was less than 1.6 eV for a pass energy of 117.4 eV.

Single-Wavelength Ellipsometry (SWE). SWE measurements were performed on a Rudolph Autoel II null ellipsometer using a wavelength of 632.8 nm and angle of incidence of 70°. Ellipsometric constants were determined for the bare gold substrates soon after removal from the deposition chamber, and new ellipsometric constants were determined after SAM formation. A three-phase model (ambient/SAM/gold) was used to calculate the SAM thickness using a refractive index of 1.50 + 0i for the SAM.⁴³

Contact Angle Goniometry. Contact angle measurements of water with the SAM surfaces were made using a Rame-Hart goniometer equipped with an environmental chamber. Water was placed into the chamber to form a saturated vapor. Reported contact angles are advancing.

External Reflectance Infrared Spectroscopy. Infrared external reflection spectra were obtained using a custom-modified BioRad-Digilab Fourier transform instrument.⁴⁴ Spectra were obtained at 2 cm⁻¹ resolution using p-polarized light at an 86° angle of incidence. Spectra were obtained with reference to a bare gold surface which was cleaned using UV/ozone and/or dilute hydrogen peroxide solutions.

Solution Formation. Supersaturated aqueous solutions were prepared to simulate physiological conditions relevant to bone growth. Since the exact solution composition at in vivo bone growth sites is not known, solutions containing multiple salts in concentrations similar to those of blood serum were used. Most of the solutions contained 137 mM NaCl, 3 mM KCl, 1.5 mM MgCl₂, 0.5 mM Na₂SO₄, 4.2 mM NaHCO₃, NaCl and CaCl₂·2H₂O varying between 2.5 and 3.2 mM, and K₂HPO₄·3H₂O in concentrations such that the ratio of total Ca²⁺ to PO₄³⁻ was 2.5. Solutions at 2.5 mM CaCl₂·2H₂O are similar to simulated body fluid solutions used previously.¹⁵ The pH was adjusted to 7.4 at 37 °C using KOH or HCl. The solutions were buffered using 1 M Tris (tris(hydroxymethyl)aminomethane) to form solutions with 0.05 M Tris and 1 M HCl to prevent CO₂ outgassing. Water was obtained from a Millipore RIOS8 and MilliQ synthesis unit with an ultrafiltration filter and ultraviolet lamp at 18 MΩ and was passed through a 0.22 μm filter. Solutions were formed by dilution from stock solutions which were filtered (0.22 μm) and standardized using inductively coupled plasma (ICP) analysis. Dissolved gases were removed from the solutions without sodium carbonate and potassium phosphate dibasic by bubbling with water-saturated nitrogen gas and by applying a vacuum to an Erlenmeyer flask containing the solutions. Degassing the solutions significantly reduced the nucleation of bubbles onto surfaces during the microbalance experiments. Sodium carbonate solutions were made fresh for each experiment and were added after degassing. Phosphate solutions were made fresh before use and were added by slow, dropwise addition. The pH was then adjusted by adding Tris buffer. Numerous other methods were used to prepare the samples including techniques used to prepare high supersaturation solutions by mixing equal volumes of calcium-containing

and phosphate-containing solutions^{25,13} and changing the order of addition of the components. Solutions were placed into jacketed beakers so that the headspace above the solution was minimized and the containers were sealed with an O-ring-containing Teflon cover or Parafilm.

Solution Analysis. Solutions were monitored for solution precipitation by examining changes in calcium and phosphate concentration using ICP and calcium ion selective electrodes. During the time course of a nucleation experiment, a sample of solution was removed and filtered using poly(ether sulfone) (MW 10,000) (~ 28 Å) ultrafiltration filters under 55 psi of nitrogen. The sample was acidified and monitored for calcium and phosphorus using ICP. An ion selective electrode and single-junction reference electrode were calibrated using solutions containing the salt background listed above, Tris buffer, and $\text{CaCl}_2 \cdot 2\text{H}_2\text{O}$ at various concentrations at 37 °C. Plots of measured potential (mV) versus log concentration were linear. Free calcium ion concentrations were determined by solution potential (mV) measurements at various times during the nucleation experiment.

Supersaturation and Speciation Calculations. Mass balance, charge balance, and chemical equations were written for the known reactions for the supersaturated solutions using reaction constants, many of which are compiled elsewhere.⁴⁵ Equations were solved numerically to determine species concentrations. Relative supersaturation values, σ , with respect to various calcium phosphate phases were determined using the equation

$$\sigma = S - 1 = (I/K_{\text{so}})^{1/\nu} - 1 \quad (1)$$

where S is the supersaturation, I is the ion activity product, K_{so} is the solubility product, and ν is the number of ions involved in the precipitation reaction. Supersaturations were calculated with respect to hydroxyapatite (HAP, $\text{Ca}_{10}(\text{PO}_4)_6(\text{OH})_2$), octacalcium phosphate (OCP, $\text{Ca}_8\text{H}_2(\text{PO}_4)_6 \cdot 5\text{H}_2\text{O}$), tricalcium phosphate (TCP, $\text{Ca}_3(\text{PO}_4)_2$), and brushite (DCPD, $\text{CaHPO}_4 \cdot 2\text{H}_2\text{O}$) using solubility products, K_{so} , of 2.35×10^{-59} ,^{9,46} 5.01×10^{-50} ,^{8,27} 2.83×10^{-30} ,^{5,47} and 2.32×10^{-7} ,^{2,48} respectively.

Quartz Crystal Microbalance. A quartz crystal oscillator housed in a Teflon probe (TPS-550 Maxtek) was connected to a power supply and a frequency counter (Stanford Research Instruments) using a triaxial cable. Data were collected from the frequency counter using a GPIB interface and a data collection and graphing program written in C. Gold electrodes were deposited onto 5 MHz AT cut 1 cm diameter polished quartz crystals (Maxtek) using 99.999% gold in a dc magnetron sputtering chamber at a 10^{-8} Torr base pressure. An ion gun was used to clean the substrates. Gold films of 2000 Å were deposited onto a 100 Å titanium or chromium adhesion layer through masks to form 0.25 in. diameter back electrodes and 0.50 in. diameter front electrodes with a tab that wrapped around to the backside. The larger electrode faced the solution and was operated at ground to avoid acoustoelectric effects. The gold films had 1000 Å grain sizes, smoothnesses, and ellipsometric constants similar to those of films formed by thermal evaporation or electron beam deposition.

The quartz crystal with gold electrodes and attached SAM was placed onto an O-ring in a receptacle in the probe so that the electrodes made contact with gold pins. A Teflon retainer was made to contain an O-ring which contacted the front of the quartz crystal. The retainer with the O-ring was used to prevent fluid from leaking into the back of the quartz crystal, which was found to occur in solutions at elevated temperatures (37 °C). A cap was screwed onto the probe base to hold the

retainer in place, and a gasket was used to prevent leakage through the retainer.

The probe was placed into a jacketed beaker thermostated with water using a NESLAB 110 microprocessor bath at 37 ± 0.01 °C. The substrates were held vertically in the solution. Companion SAM wafer samples were also placed into the solutions oriented vertically and horizontally. Supersaturated solutions were poured into the beaker, the solutions were stirred at controlled rates, and frequency data were collected at various time intervals with a 1 s gate time per measurement. Results from 5–10 measurements were averaged. In some cases, two probes were placed into the same solution and frequency change data were collected simultaneously. The resonance frequency of the quartz crystal changes upon introduction into solution from air due to a viscous component of the frequency change as described by Kanazawa.⁴⁹ This component is subtracted by obtaining baseline frequency readings in solution. Changes in frequency after the baseline was achieved were attributed to changes in mass due to deposition of calcium phosphates and were analyzed by the Sauerbrey equation.⁵⁰

An HP 4194A impedance/gain phase analyzer and HP 41941 impedance probe were used to determine the impedance phase and magnitude as a function of applied frequency over a span of 20 kHz from the series resonance frequency, f_s , for several of the nucleation kinetic experiments. Motional resistance, R_m , values were determined over time using a Butterworth–vanDyke equivalent circuit analysis.⁵¹

Adsorbate Studies. XPS Studies. Adsorbates in the initial stages of nucleation and growth were studied by quantitative analysis of O 1s, Ca 2s, Ca 2p, P 2p, and C 1s peak areas. Standard HAP, TCP, and OCP powders were also examined. In some cases, especially for the powders and thicker films on SAMs on gold, charging was compensated by neutralization using an electron flood gun. Since the Au 4f_{7/2} peaks from the substrate overlapped with the Ca 2p peak, the Ca 2s peak was used to quantify calcium in the films.⁵² The Ca/P ratios of the films were then normalized to Ca/P ratios of standard calcium phosphate powders since calcium deficiency occurs in XPS studies of calcium phosphate films and standard powders^{29,53} due to beam damage.⁵⁴ In addition, we avoided use of sensitivity factors and determined the Ca 2s/P area ratios of peaks and standardized them to Ca 2s/P area ratios of standard powders.

For these analyses, samples were removed from the nucleating solutions, briefly rinsed in 1 mL of water to remove residual salt solution, and dried using a flow of nitrogen at 10 psi. Further water rinsing resulted in a reduction in the amount of deposit detected but no significant changes in the deposit composition.

TOF-SIMS. Adsorbates in the initial stages of nucleation and growth were studied using (Cs)Cs⁺ projectiles formed by a ²⁵²Cf radioactive source.⁵⁵ The projectiles were accelerated to a 20 keV impact energy. Negative secondary ions were accelerated to −7 keV and mass analyzed by time of flight. This technique has been shown to be effective for characterizing various calcium phosphate phases in minute quantities⁵⁴ and calcium phosphate crystal growth⁵⁶ by examining emitted PO_3^- / PO_2^- ratios.

Calcium Phosphate Film Characterization. In addition to the microbalance studies, the amounts of deposited calcium phosphate were verified using single-wavelength ellipsometry. A three-layer model (ambient/calcium phosphate film/SAM on gold) was used to determine the calcium phosphate film thicknesses using a refractive index of 1.6, which is an average of reported values for HAP and OCP. Film amounts were also characterized by dissolution of films using concentrated HCl

and determination of calcium and phosphorus concentrations using ICP analysis.

Glancing Angle XRD. The diffraction apparatus used was a Philips X'Pert MPD system (PW 3040/00 type) with a vertical θ/θ goniometer (220 mm radius) and a fixed-anode (Cu LFF) sealed ceramic tube X-ray source operated at 40 kV and 50 mA (2.0 kW). The incident beam optics included an automatic divergence slit, a 0.04 rad soller slit, and a brass beam mask. The receiving optics consisted of a 0.27 rad plate collimator, a flat graphite monochromator, and a proportional counter detector. The divergence slit and beam mask limited the study area on each specimen. The incident beam was fixed at grazing incidence (Ω) of 5.0° , and the scan axis was 2θ . Spectra were taken at rates of $0.05^\circ/2$ s and $0.05^\circ/60$ s.

FEM. Images of films were obtained using a LEO 982 field emission scanning electron microscope operating at a resolution of 1 nm at 30 kV and 4 nm at 1.0 kV. The scope was operated at 3 kV, and most of the pictures were taken with the below-lens (ET) secondary electron detector. A few images were mixed signals from the ET and in-lens secondary electron detector.

AFM. Substrates for AFM studies were prepared by resistive evaporation of gold (99.999%) onto the surface of freshly cleaved mica which was preheated in a vacuum to 340°C . A 2000 Å film of gold was deposited, and the substrate temperature was returned to $<40^\circ\text{C}$ under vacuum. Images of the films were obtained using a Digital Instruments Nanoscope IIIa instrument in tapping mode using a small-area scanner. The images were obtained at a 0.5–1.0 Hz scan rate and were the first images obtained with a fresh Nanodevices Tap300 micro-machined silicon tip operating at around 300 kHz. Particle height and diameter values were obtained by section analysis of the images.

Results

Self-Assembled Monolayer Characterization. Characterization of the SAMs indicated the formation of monolayers with the expected structures and surface properties as described previously.³⁴ The monolayers had high degrees of organization as evidenced by the C–H stretching modes at $\sim 2918\text{ cm}^{-1}$ (CH_2 , antisymmetric (d^-)) and 2850 cm^{-1} (CH_2 , symmetric (d^+)). Contact angles were $<10^\circ$, 20° , and $110^\circ \pm 2^\circ$, and ellipsometric thicknesses were 23, 22, and 21 ± 1 Å for the COOH, OH, and CH_3 SAMs, respectively.

Nucleation and Growth Kinetics. Figure 1a shows kinetic data for the nucleation and growth of calcium phosphate onto COOH SAMs from solutions at two supersaturations as determined by quartz crystal microbalance measurements. The data represent real time data from several representative experiments. Calcium ion concentrations in solution were monitored by a calcium ion electrode as shown in Figure 1b. Supersaturations were varied by changing the calcium and phosphate concentrations and keeping the concentration of the other salts constant to maintain constant ionic strength. Table 1 shows the solution composition and calculated initial supersaturations of the solutions with respect to DCPD, OCP, TCP, and HAP. Plots in Figure 1a revealed an initial induction period followed by a second region of extensive growth. The duration of the induction period was quite long, amounting to 11–14 days, and increased with decreasing supersaturation of the solutions. The variability in the induction times over six repeated experiments was $\sim 20\%$.

The growth rate in the second region reached a maximum constant value for a 4 h time period and then slowly decreased over time until a plateau region occurred at about 48–72 h.

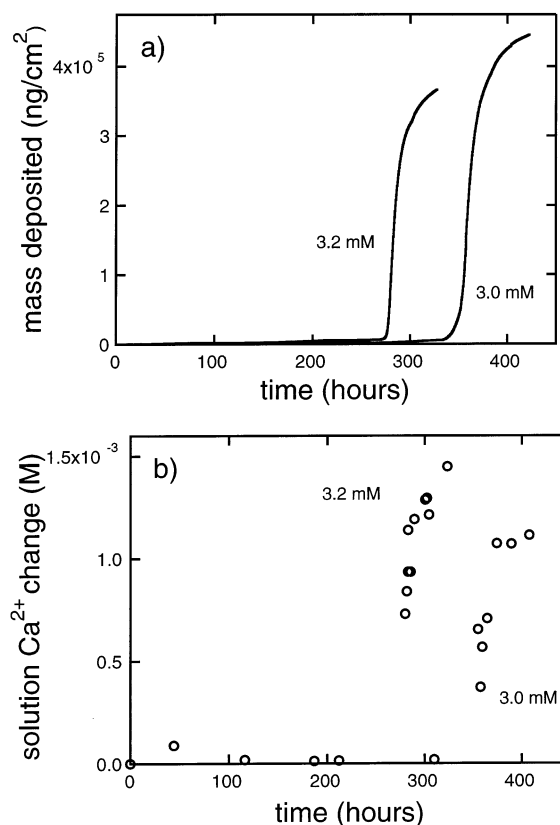


Figure 1. (a) Quartz crystal microbalance determined calcium phosphate deposition kinetics onto COOH SAMs from supersaturated solutions shown in Table 1 at 3.0 and 3.2 mM $\text{CaCl}_2 \cdot 2\text{H}_2\text{O}$. (b) Changes in Ca^{2+} concentration in solution for the same solutions at 3.0 and 3.2 mM $\text{CaCl}_2 \cdot 2\text{H}_2\text{O}$.

TABLE 1: Initial Compositions and Relative Supersaturation Values, σ , with Respect to DCPD, TCP, OCP, and HAP for Solutions Used in This Work

$[\text{CaCl}_2 \cdot 2\text{H}_2\text{O}]$ (mM)	$[\text{K}_2\text{HPO}_4 \cdot 3\text{H}_2\text{O}]$ (mM)	$\sigma(\text{DCPD})$	$\sigma(\text{TCP})$	$\sigma(\text{OCP})$	$\sigma(\text{HAP})$
3.0	1.20	−0.407	3.82	2.37	19.0
3.2	1.28	0.025	4.14	2.57	20.2

The growth rates in the linear region were $400\text{ ng}/(\text{cm}^2\text{ min})$ ($14\text{ Å}/\text{min}$ assuming the deposits have a density of $3.0\text{ g}/\text{cm}^3$) and $330\text{ ng}/(\text{cm}^2\text{ min})$ ($11\text{ Å}/\text{min}$) for the 3.2 and 3.0 mM $\text{CaCl}_2 \cdot 2\text{H}_2\text{O}$ solutions, respectively. The final amount of calcium phosphate deposited onto the SAMs was higher for data shown in Figure 1a for the 3.0 mM solution versus 3.2 mM solution; however, there was no statistically significant difference over the experimental repetitions performed. The variability in the growth rates and amounts deposited over repeated experiments was in the range of 20–25%. The final amounts deposited corresponded to calcium phosphate thicknesses of $\sim 1.5\text{--}2.5\text{ }\mu\text{m}$. Impedance studies of deposition showed no significant changes in motional resistance, R_m , indicating that the resonance frequency decreases corresponded to masses that were rigidly coupled and did not involve changes in viscous coupling due to viscoelastic adsorbates or changes in interfacial viscosity.

Figure 1b shows data for changes in the concentrations of free Ca^{2+} obtained from calcium ion specific electrodes obtained simultaneously with the surface kinetic data in Figure 1a. The data are expressed in terms of calcium concentration changes from the original solution. Note that there were no significant changes in solution calcium concentrations during the initial induction period. The decreases in calcium ion concentrations after the induction period coincided with calcium phosphate

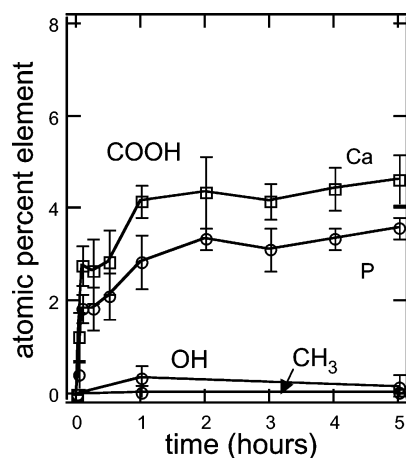


Figure 2. Atomic percent Ca and P as determined from XPS Ca 2s and P 2p peak areas for early induction period deposits on COOH SAMs exposed to 3.2 mM $\text{CaCl}_2 \cdot 2\text{H}_2\text{O}$ solutions.

deposition onto the COOH SAMs as determined by the microbalance technique. Similar calcium ion concentration decreases were seen for solutions that did not contain SAM substrates. ICP analyses of solutions removed and filtered after various time periods also showed decreases in calcium and phosphorus concentrations. Changes in the rate of calcium ion depletion in solution corresponded to changes in the rate of growth onto the SAMs, both showing a growth rate plateau after 48–72 h. The total amount of calcium phosphate formation due to calcium ion depletion in solution exceeded the amount of deposition on the surfaces by a factor of ~ 150 –200.

XPS and TOF-SIMS Adsorbate Studies. Insignificant amounts of deposition can be observed in the initial induction period in expanded views of the microbalance data. This deposition was observed as soon as the substrates were exposed to the supersaturated solution and was studied in greater detail using XPS and TOF-SIMS analyses. Figure 2 shows quantitative XPS data for SAM substrates exposed to 3.2 mM $\text{CaCl}_2 \cdot 2\text{H}_2\text{O}$ solutions for the first 5 h of deposition in Figure 1. The data show that adsorbates containing calcium and phosphorus were observed as soon as the COOH templates were exposed to the solutions. There was a relatively fast increase in calcium and phosphorus amounts up to 30–60 min, and a relatively slow rate of increase in deposition after that time. Ellipsometry measurements indicated that the equivalent thickness of deposit at the plateau or saturation point was ~ 10 –15 Å.

Corrected Ca/P ratios for the deposits in Figure 2 were initially ~ 1.40 and then decreased to ~ 1.30 after 5 h. This ratio indicates that the deposits in the initial induction period were not adsorbed cations such as Ca^{2+} or soluble calcium phosphate species such as CaHPO_4 , $\text{CaH}_2\text{PO}_4^+$, and CaPO_4^- , which were present in the solutions as determined by speciation calculations, but must be a polynuclear complex or insoluble particle such as $\text{Ca}_8\text{H}_2(\text{PO}_4)_6 \cdot \text{H}_2\text{O}$ or $\text{Ca}_3(\text{PO}_4)_2$. The effect of nucleating template functionality on deposits during the induction period was also examined by XPS in Figure 2. The COOH functional groups promoted significantly more deposition compared to the OH and CH_3 functional groups. A similar effect of functional group was shown for early deposition from solutions containing K_2HPO_4 as the phosphate source.⁵⁷

To obtain further information on the chemistry of the initial adsorbate, a TOF-SIMS technique was used which obtains ratios of $\text{PO}_3^-/\text{PO}_2^-$ emitted from the substrates after bombardment with $(\text{CsI})\text{Cs}^+$ projectiles. The TOF-SIMS technique is sensitive to small amounts of adsorbates as the use of a polyatomic

TABLE 2: $\text{PO}_3^-/\text{PO}_2^-$ Ratios Obtained from TOF-SIMS Studies of Early Calcium Phosphate Deposits in the Induction Period onto COOH SAMs Exposed to Supersaturated Solutions for Various Time Periods^a

[$\text{CaCl}_2 \cdot 2\text{H}_2\text{O}$] (mM)	time in solution (h)	$\text{PO}_3^-/\text{PO}_2^-$	phase with closest $\text{PO}_3^-/\text{PO}_2^-$ ratio
2.5	2	0.97	OCP (1.08)
2.5	24	1.00	OCP
2.8	2	1.00	OCP
2.8	24	.87	HAP (0.84)

^a The standard calcium phosphate phase with the closest $\text{PO}_3^-/\text{PO}_2^-$ ratio is listed.

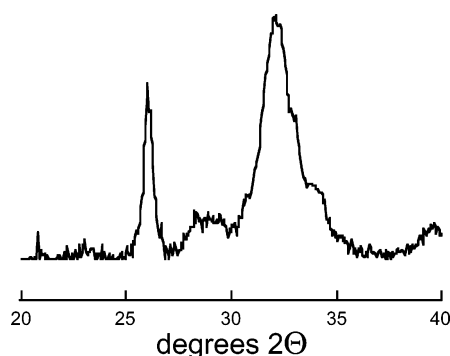


Figure 3. Glancing angle X-ray diffraction spectra of a film formed from a 3.2 mM $\text{CaCl}_2 \cdot 2\text{H}_2\text{O}$ solution onto a COOH SAM.

projectile increases the yield of emitted polyatomic ions. The ratio of PO_3^- to PO_2^- emitted has been found to vary with calcium phosphate structure and phase.^{54,58} Table 2 shows $\text{PO}_3^-/\text{PO}_2^-$ ratios for COOH SAMs exposed to supersaturated solutions. The solution conditions were slightly different (lower supersaturation) from those used for the deposition kinetic studies in Figures 1 and 2. These studies indicated that the initial deposits had $\text{PO}_3^-/\text{PO}_2^-$ ratios of ~ 1.0 after exposure to 2.5 and 2.8 mM $\text{CaCl}_2 \cdot 2\text{H}_2\text{O}$ solutions. These ratios are similar to those seen for standard powders of OCP ($\text{PO}_3^-/\text{PO}_2^-$ ratio of 1.08).⁵⁴ The $\text{PO}_3^-/\text{PO}_2^-$ ratios remained constant after 24 h for deposits from 2.5 mM $\text{CaCl}_2 \cdot 2\text{H}_2\text{O}$ solutions, but $\text{PO}_3^-/\text{PO}_2^-$ ratios decreased to 0.87 for deposits from 2.8 mM $\text{CaCl}_2 \cdot 2\text{H}_2\text{O}$ solutions. This ratio is similar to $\text{PO}_3^-/\text{PO}_2^-$ ratios found for HAP standards (0.85).

Film Phase and Morphology. Figure 3 shows glancing angle X-ray diffraction spectra for films after the growth period was completed. A relatively sharp peak occurred at 26° and a broader peak in the region of 31 – 34° , which are consistent with (002) and (211), (112), and (300) reflections of apatite, respectively. There is some degree of line broadening for the peaks at 31 – 34° , suggesting small crystallite sizes. The (002) reflection had a higher intensity than that predicted for a random orientation of apatite, which indicated some degree of (002) orientation, resulting in the c axis being perpendicular to the substrate. XPS showed that the films had Ca/P ratios of 1.46, which are consistent with the formation of apatite with a small degree of calcium deficiency.

Figure 4 shows AFM and FEM images of films grown onto COOH SAMs from solutions at 3.0 mM $\text{CaCl}_2 \cdot 2\text{H}_2\text{O}$ at various stages during the initial induction period and second growth period. The AFM image in Figure 4a was obtained on a COOH SAM after exposure to the supersaturated solution after 40 h in the induction period. The SAM was assembled onto gold deposited onto mica. The image shows typical features for gold deposited onto mica such as several 0.5 – $1 \mu\text{m}$ gold terraces separated by ~ 30 – 50 Å step edges. There are also defect pits

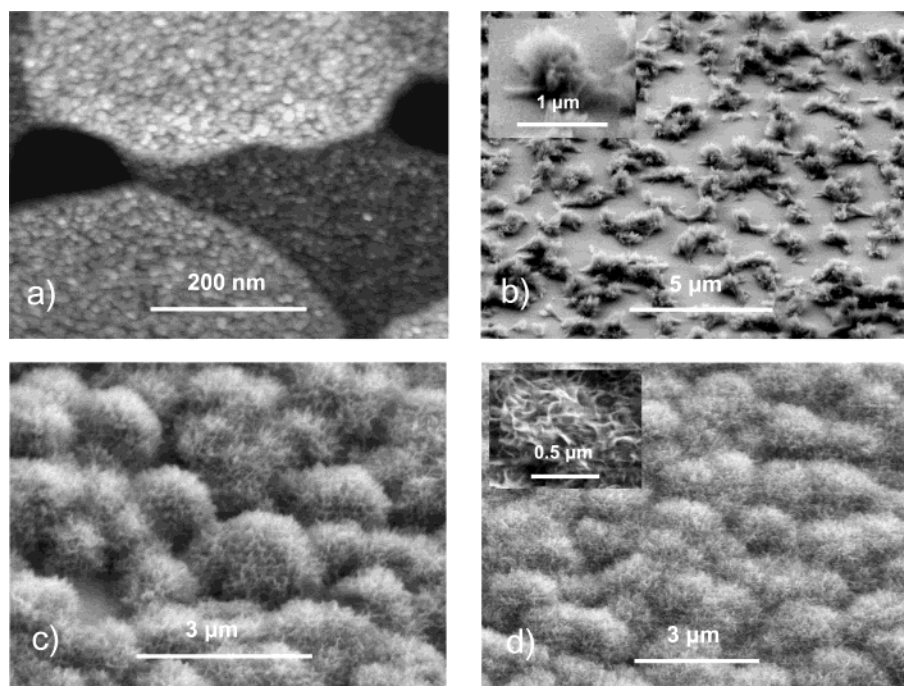


Figure 4. AFM and FEM images (45° tilt angle) of calcium phosphate deposition from 3.0 mM $\text{CaCl}_2 \cdot 2\text{H}_2\text{O}$ solutions at various times during the deposition shown in Figure 1: (a) top AFM view of a nanoparticle monolayer on a SAM on gold on mica 40 h into the induction period, (b) FEM image after 353 h, 13 h into the growth region (the inset is a 45° tilt angle view at higher magnification), (c) FEM image after 358 h, 18 h into the growth region, (d) FEM image after 393 h, 53 h into the growth region (the inset is a planar view at higher magnification).

that are ~ 1000 Å deep. The picture shows very small ~ 185 Å diameter by ~ 15 Å height particles on top of the surface. The particles are densely packed onto the surface and appear to form a near monolayer. There appeared to be no significant deposition onto the surfaces besides the nanoparticle layer until the onset of the growth region. Several hours after the onset of the growth region, crystallites that were ~ 1000 Å were observed. Figure 4b shows a 45° tilted FEM image after ~ 13 h of the growth period. The image shows isolated crystallites with an average diameter of ~ 0.9 μm . The high-magnification inset indicates that the crystallites consist of platelike substructures, many of which appear to be oriented perpendicular to the substrate. Figure 4c shows an image after 18 h of growth which shows a film consisting of larger, ~ 1.3 μm crystallites that are nearly coalesced with adjacent crystallites. The crystallites appear to be discrete, and there are some spaces between adjacent crystallites. Figure 4d shows an image after 53 h of growth showing a dense, coalesced film consisting of ~ 1.6 μm crystallites. The crystallites appear less discrete, indicating more extensive growth between the individual crystallites. Images of cross sections showed that the films increased in thickness up to ~ 2.0 μm after the crystallites coalesced. The high-magnification inset in Figure 4d shows a top view of the crystallites showing the platelike substructures which are 1000–2000 Å in diameter.

Discussion

Nucleation Mechanism. The solution and deposition studies show that growth of calcium phosphate onto self-assembled monolayers from physiological-like solutions involves the adsorption of solution-formed crystallites. The adsorption of a solution-formed particle is an alternative mechanism to heterogeneous nucleation involving formation of the critical nucleus onto the substrate. To our knowledge, a mechanism involving solution-formed nuclei has not been shown previously for calcium phosphate.

We will briefly summarize this mechanism shown schematically in Figure 5 and then discuss it in greater detail below. First, a long induction period occurred that lasted 11–14 days depending on the solution supersaturation. There was a very small amount of deposition during this period due to the adsorption of nanoparticles which were present as artifacts in the as-made solutions. The nanoparticle monolayers are not shown in the Figure 5 schematic for clarity, although we depict the nanoparticle adsorption mechanism in detail elsewhere.⁵⁷ Next, at the onset of the growth region, critical nuclei formed in the solutions as shown schematically in Figure 5b. The nuclei start to grow and adsorb onto the substrates at various stages of growth (Figure 5c), and then they grow further on the substrates until they have coalesced with adjacent crystallites as shown in Figure 5d.

Initial Induction Period. First, we will discuss the deposits found during the initial induction period. The deposits were insignificant (10–30 Å) and easily overlooked, but the mechanism of deposition is interesting and unexpected. We briefly touch on the mechanisms here and provide more details in a subsequent paper. The deposits occur due to the adsorption of nanoparticles. The nanoparticles are present in the as-made solutions as evidenced by a decrease in concentration of calcium and phosphate in the solutions after filtering them using ultrafiltration filters. The ion depletion experiments showed very dilute particle concentrations on the order of 10^{-5} to 10^{-6} M calcium phosphate. It was not possible to detect the nanoparticles using small-angle X-ray scattering due to their low concentration and the high ionic strength of the solutions, although we did observe scattering from a HeNe laser by the eye. AFM studies of adsorbates onto COOH SAMs on gold on mica in Figure 4a showed the presence of 185 Å diameter by ~ 15 Å thickness nanoparticles. Adsorbed nanoparticles were also observed from supersaturated solutions containing K_2HPO_4 as the phosphate source⁵⁷ and simpler, nonphysiological solutions that contained calcium and phosphate salts and NaCl only. AFM overestimates

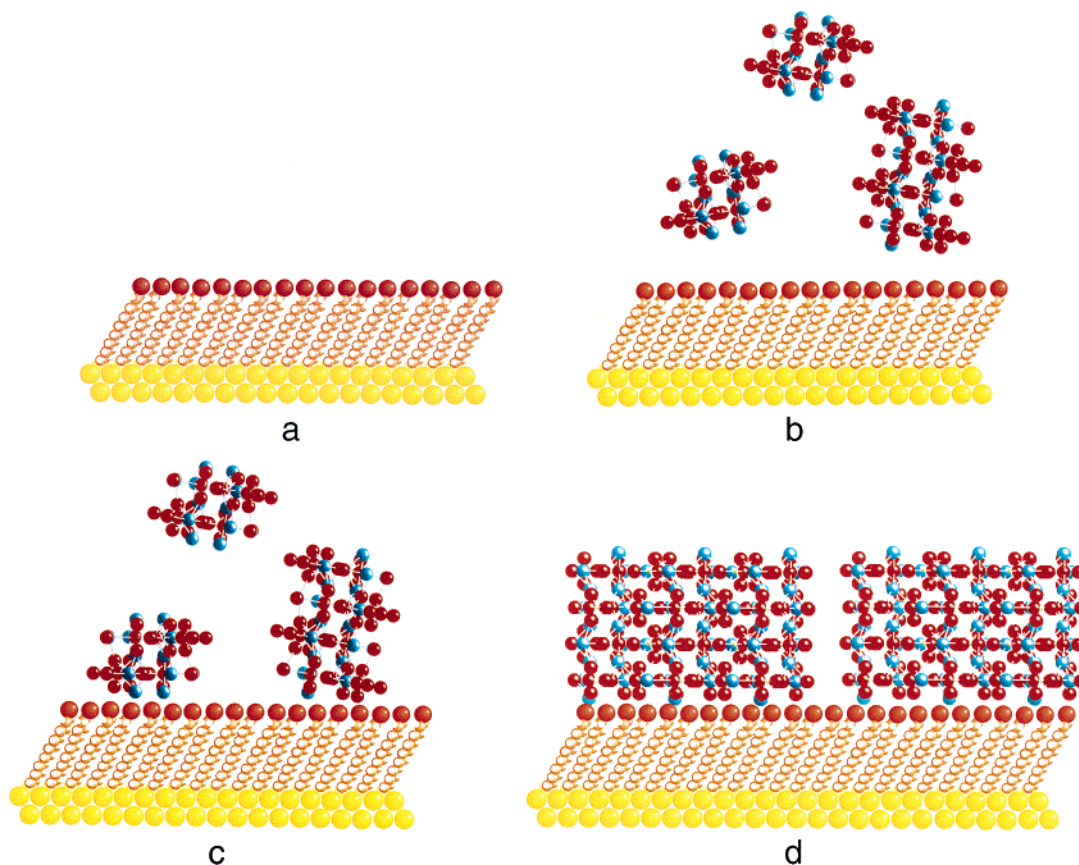


Figure 5. Schematic drawing of the nucleation and growth mechanism for calcium phosphate physiological solutions showing (a) the substrate in solution during the induction period (note that nanoparticle adsorption observed during the induction period is not shown in this schematic for clarity), (b) formation of calcium phosphate critical nuclei in solution at the onset of the growth region, (c) adsorption of growing crystallites onto the substrates, and (d) growth and coalescence of crystallites to form (001)-oriented HAP crystallites on the surface. Atom colors: hydrogen, white; carbon, brown; oxygen, red; calcium, blue; sulfur, yellow; gold, yellow/orange.

the true diameter due to tip artifacts so that the real diameter may be smaller by a factor of 2 or 3 as shown in previous studies of gold nanoparticles.⁵⁹ The particles are larger than the 8–10 Å Posner-type clusters suggested to exist in some supersaturated solutions.⁶⁰ We are using the term “nanoparticle” to describe these small adsorbates to distinguish them from smaller molecular “clusters”.

The origin of the nanoparticles in the as-formed solutions deserves some discussion. We believe that the nanoparticles form as an artifact of the solution formation process because of local increases in the solution concentration due to the addition of phosphate-containing solutions or base to dilute calcium-containing solutions. Supercritical particles may form which are irreversible and do not dissolve. Numerous studies were done to vary the solution formation process to reduce the nanoparticles including changing the order of addition of reactants and the method of mixing calcium- and phosphate-containing solutions. Addition of concentrated phosphate stock solutions to dilute calcium-containing solutions, concentrated calcium stock solutions to dilute phosphate-containing solutions, or concentrated base to calcium- and phosphate-containing solutions tended to increase the nanoparticle concentrations and adsorption amounts. The nanoparticle concentrations were reduced by forming equal volumes of calcium-containing and phosphate-containing solutions at the final pH and ionic strength and mixing the two solutions simultaneously. These effects are consistent with the idea that the particles are being formed as artifacts of the solution formation process because of local concentration gradients. The nanoparticle concentrations were also reduced by filtering the final solutions with ultrafiltration filters. Although we were

unable to completely eliminate these particles, their existence is real and was previously overlooked.

The initial nanoparticle adsorption resulted in deposition amounts that are insignificant compared to those of the growth region, yet the adsorption has profound effects on changing the interfacial chemistry. These changes may significantly affect or limit heterogeneous nucleation processes. Even low particle concentrations resulted in the adsorption of a monolayer or near monolayer of nanoparticles which blocked the underlying COOH sites. Although solution conditions were used to minimize nanoparticle formation in this study, we have also purposely used solution conditions that promote nanoparticle formation as an interesting way to form ultrathin films of calcium phosphate.⁵⁷ Previous literature has shown small amounts of calcium phosphate deposited in an initial induction period and images of nanosized deposits which may be explained by this nanoparticle adsorption mechanism.^{21,29,56,61}

Growth Region. After the long induction period, critical nuclei precipitated in solution, started to grow, adsorbed onto the surfaces, and then grew further to form films as shown schematically in Figure 5. The formation of nuclei in solution was evidenced by calcium ion depletion in the solutions (shown in Figure 1b), which corresponded directly with deposition onto the surfaces (Figure 1a). The calcium ion depletion corresponded to solution precipitation and not heterogeneous nucleation of calcium phosphate onto the COOH SAMs because heterogeneous nucleation alone would result in no detectable calcium ion depletion because of the low surface areas and large solution volumes used. The calcium ion reduction corresponded to the formation of apatite approximately 150–200 times in excess

of the amount of apatite grown on the surfaces. Solution precipitation as evidenced by calcium ion depletion also occurred in companion solutions that did not contain nucleating substrates. The onset of the growth region was identical for multiple SAM substrates placed into the same supersaturated solution, which is consistent with a solution-formed nucleus mechanism but would be unlikely for heterogeneous nucleation after such long induction times. Calcium phosphate was deposited onto SAM substrates that were placed into the solutions after the onset of calcium depletion; this result is also indicative of a solution-formed nucleus mechanism. Solution precipitation was also evidenced by observations of increased HeNe laser scattering. Growth of films by this mechanism occurred onto surfaces that were oriented vertically and horizontally in the supersaturated solutions.

The initial induction period, therefore, represented an induction time period for the formation of nuclei in solution. This period is typical of nucleation and growth behavior and occurs because there is an activation energy required for nucleation, ΔG^* , which depends on the interfacial energy for formation of the nucleus, γ , and the solution supersaturation, S . An expression for the induction time, τ , as described by classical nucleation theory is

$$\tau = \frac{N^*}{J} = \frac{N^*}{\Omega} \exp\left(\frac{\Delta G^*}{kT}\right) = A \exp\left(\frac{\beta v^2 \gamma^3}{(kT)^3 (\ln S)^2}\right) \quad (2)$$

where N^* is the nucleation density, J is the nucleation rate, Ω is a preexponential factor, β is a shape factor, and v is the molecular volume. This equation predicts that the induction time is diminished and nucleation promoted by reducing the solid/solution interfacial tension, γ , or by increasing the supersaturation, S . The effect of increasing the supersaturation on reducing the induction time was observed experimentally in Figure 1.

We are using the terms “solution formation” and “solution-formed” nuclei instead of “homogeneous nucleation” to include the possibility that the nuclei form on impurities present in the solutions. In fact, the presence of dilute concentrations of nanoparticles in the initial solutions suggests this possibility. At the present time, we have no clear knowledge of whether the nanoparticles present in the as-formed solutions or other components such as the Tris buffer influenced solution nucleation. Solution nucleation did not occur for experiments we did with K_2HPO_4 -containing solutions even though nanoparticles were in the as-formed solutions, but the initial particles were more highly defected and calcium deficient than the initial nanoparticles in the $K_2HPO_4 \cdot 3H_2O$ -containing solutions and may not have been as good of nucleating substrates. On the other hand, the less defected nanoparticles in the $K_2HPO_4 \cdot 3H_2O$ -containing solutions adsorbed onto the SAM surfaces but did not promote significant nucleation onto the surfaces.

At the onset of the growth region, nuclei formed in the solution, started to grow, and adsorbed onto the substrates, the substrates having nanoparticle monolayers on top of the COOH SAMs. We do not have knowledge of the distribution of sizes of the crystallites once adsorbed, but they probably include critical nuclei and postcritical particles at various stages in the growth process. The smallest particle depicted in the schematic in Figure 5b is ~ 10 Å in size, which is on the order of critical nucleus sizes (10–20 Å) expected for slightly soluble salts such as calcium phosphate. After adsorption, further growth of crystallites on the surfaces is indicated by the increasing crystallite sizes over time shown in Figure 4. The crystallites stop growing laterally after coalescence occurred by ~ 18 h, but

continue to grow in the vertical direction. The schematic in Figure 5d depicts two crystallites that have grown and coalesced.

At the same time that adsorbed crystallites are growing on the substrates, crystallites are also growing in solution. The experiments showing calcium and phosphate depletion in solution suggest that growth occurs by consumption of ions and their incorporation into a solid lattice. The changes in the growth rate of calcium phosphate onto the SAMs determined by the microbalance were similar to the changes in the growth rate of calcium phosphate in solution as determined by calcium depletion, suggesting that the growth mechanisms are the same, involving ion-by-ion growth of nuclei. There is a possibility that part of the growth onto the substrates involves crystallites growing in solution aggregating onto crystallites growing on the surfaces. Crystallite aggregation is sometimes involved in the solution formation of colloidal particles. The aggregation rates of growing particles, however, are reduced if the particles are charged and if dilute solutions are used. We believe deposition of calcium phosphate onto the SAMs was dominated by growth of crystallites over aggregation of crystallites because of growth rates similar to solution crystallite growth rates and high crystallinities in the [001] direction. In addition, there was no significant change in crystallite diameter after film coalescence occurred, only growth perpendicular to the substrate, which is also suggestive of ion-by-ion growth. At later time periods, especially in the late plateau region after 24–47 h shown in Figure 1, several globular crystallites were observed on top of the underlying film. These crystallites were larger than the crystallites within the film and are most likely crystallites that grew in solution and then attached onto the substrate. The extent of aggregation from solution, however, was very limited.

Although the solution studies showing depletion of calcium and phosphate ions indicate that growth occurs by ion-by-ion incorporation, there has been some recent suggestion of the possibility of calcium phosphate growth by the incorporation of small calcium phosphate clusters.^{53,60,62,63} Growth by aggregation of polynuclear clusters or oligomers has been found in oxyhydroxides such as FeOOH and AlOOH. A small 7–10 Å molecular cluster has been observed by dynamic light scattering using an argon laser and proposed to be similar to $Ca_9(PO_4)_6$; however, this cluster has not been isolated and identified chemically.⁶⁰ Previous studies showed no change in solution supersaturation during the time period that cluster incorporation was suggested to occur, indicating that the clusters are in the as-made solution.⁵³ Once the clusters are formed they are stable and do not grow except by aggregation with other clusters. Since significant growth onto the SAM in our studies is associated with calcium and phosphate depletion, the only way to reconcile a cluster incorporation growth mechanism would be if the calcium and phosphate depletion observed corresponded to nucleation of these clusters. Nucleation of slightly soluble salts such as calcium phosphate does not usually occur over time periods as long as 24–72 h, however, as it is usually burst-type with growth quickly dominating over nucleation. If the growth data onto the SAM surfaces shown by the microbalance data represent growth due to aggregation of clusters, we would not expect the growth rate changes to be the same as the nucleation rate of clusters, hypothetically represented by the calcium depletion rates in solution. Growth in our solutions, therefore, is most reasonably explained by ion-by-ion incorporation into critical nuclei formed at the onset of the growth region.

The growth rate started to decrease after time periods of 24–

48 h, which is attributed to a reduction in solution supersaturation with depletion of ions and species due to precipitation. Although the supersaturations decreased, the solutions were still supersaturated with respect to TCP, OCP, and HAP at the end of the experiment.

The apatite films may have formed by transformation of initially formed OCP nuclei in the growth region. The films have high degrees of (002), *c* axis orientation, as shown by the X-ray diffraction data in Figure 3, and the plates are oriented perpendicular to the substrate, as shown by the FEM images in Figure 4. Platelike structures are typical of OCP with the plates occurring in the "*bc*" plane of the unit cell. *c* axis orientation corresponding to plates which are perpendicular to the substrate, therefore, would be consistent with precursors with OCP crystal structure and morphology. OCP transforms to apatite topotactically, keeping the *b* and *c* axes and the platelike morphology of the original OCP crystal.⁶⁴ The plates eventually develop gaps along the *c* axis which split to form apatite needles. Crystallinity is retained for this transformation because it does not involve dissolution. The calcium deficiency in the apatite films ($\text{Ca/P} = 1.46$) is also typical of apatite formed by transformation from OCP ($\text{Ca/P} = 1.33$) which involves incorporation of calcium. It is also possible that the platelike morphology is promoted by the adsorption of ions such as carbonate.⁶⁵ Further work is necessary to confirm whether OCP precursors occur.

The high degree of (002) orientation is interesting for growth involving a solution-formed nucleus mechanism. The orientation is most likely due to the preferred growth direction of OCP and HAP along the *c* axis. Orientation along preferred growth directions is common in thin film synthesis in vapor or aqueous systems. Exaggerated growth of plates in the perpendicular direction relative to other directions is shown in the high-magnification inset of Figure 4b. Alternatively, the orientation may be due to the adsorption of the nuclei in a preferred orientation with respect to the substrate. This would occur by electrostatic interactions between the negatively charged template and positive faces on the nucleus. It seems unlikely, however, that the platelike crystallites would adsorb edge-on with plates perpendicular to the substrate since hydrodynamic forces would push the plates face down. We view the preferred growth direction as a more reasonable mechanism for the (002) orientation.

Factors Limiting Heterogeneous Nucleation on SAMs. In addition to studies with solutions similar to physiological solutions, a large number of nucleation experiments were done using simpler, nonphysiological solutions containing calcium, phosphate, and sodium chloride salts only. Experiments were done using $\text{Ca}(\text{NO}_3)_2$ instead of $\text{CaCl}_2 \cdot 2\text{H}_2\text{O}$, various phosphate sources such as KH_2PO_4 , low- and high-ionic-strength solutions adjusted with sodium chloride, and solutions over a range of supersaturations as low as 0.2–2 mM Ca^{2+} . Solutions were at pH 7.4, had calcium/phosphate ratios of 1.67, and were supersaturated with respect to just HAP or OCP, TCP, and HAP, but not DCPD. There was no significant growth of calcium phosphate using these solutions, although small amounts of heterogeneous nucleation and growth may have occurred that were not detectable by the microbalance technique. The lower supersaturation solutions exhibited no significant changes in pH or Ca^{2+} concentration over the time periods examined. Solution precipitation did occur in the nonphysiological solutions at higher supersaturation values, which resulted in growth onto SAM substrates by a similar mechanism described in this work for physiological solutions.⁶⁶ In general, there was no significant nucleation and growth onto the SAMs from solutions that did

not exhibit some evidence for solution formation of nuclei during the time course of the growth experiment.

Strong evidence for heterogeneous nucleation has been found in previous work using solutions at relatively low supersaturations containing calcium salts, KH_2PO_4 , and background electrolyte.^{27,28} These studies, in general, monitored solutions for solution precipitation before substrates were introduced using a pH stat in the constant-composition method. No precipitation occurred over long time periods until nucleating particles or molecules were added. Heterogeneous nucleation of HAP and/or OCP was demonstrated onto high-surface-area suspensions of titania particles,^{23,27,61} phosphated polymers,²⁵ carboxylated polymers,²⁶ and surfactants.²⁸

It is not clear why the planar, low-surface-area SAM surfaces do not promote significant heterogeneous nucleation of HAP compared to the suspension systems used previously. The growth rates seen in the suspension systems when normalized for surface area are easily detected by the microbalance technique. The adsorption of a monolayer of nanoparticles onto the planar SAMs in the initial induction region may block heterogeneous nucleation sites. The suspension systems have high concentrations (e.g., ~ 0.3 M titania) and may not be affected by initial nanoparticles present at much lower concentrations (10^{-6} M calcium phosphate). The SAM templates composed of high densities of negatively charged functional groups may be less effective nucleators than individual surfactant or polymer molecules containing one or two functional groups. This may occur because SAM templates have larger electrostatic double layers which may limit anion interactions at the interface compared to individual molecules. Negatively charged surfaces may not promote phosphate adsorption in contrast to titania surfaces which have been found to adsorb both calcium and phosphate.⁶¹ In addition, SAMs have restrictive geometries (hexagonal close packed) and headgroup site spacings (4.97 Å) which may limit structural promotion of nucleation. It has been previously suggested that calcium carbonate nucleation is better promoted by proteins in solution in contrast to organized molecular templates.⁶⁷ Growth of calcium phosphate onto the SAMs, therefore, required use of solutions with relatively high supersaturations that resulted in solution-formed nuclei.

A solution-formed critical nucleus mechanism may be relevant to some of the previous studies using physiological-type simulated body fluid solutions.^{16,29,68} Solution precipitation has not been examined in many of these studies. The supersaturation of our solutions at 3.2 mM CaCl_2 is similar to the supersaturation of "1.5SBF" solutions used previously.⁶⁹ The long induction times we observed before significant deposition are consistent with the long time periods necessary to grow films from simulated body fluid solutions. The globular grains and platelike substructures shown in Figure 4 are similar to microstructures shown in the literature. A couple of studies have shown decreases in calcium and phosphorus concentrations in solution which may be due to the formation of solution-formed nuclei.^{70,71} Solution precipitation may have been promoted in simulated body fluid solutions containing glass substrates or beads by nucleation onto silicate species leached from the glass.^{17,21,68,69,72} Calcium phosphate nucleation has been related to the onset of dissolution of silica, suggesting nucleation occurs onto dissolved silicate species but not the silica substrate.^{71,73} Heterogeneous nucleation may be involved in some of the previous simulated body fluid studies, especially those at lower supersaturation, but it would be necessary to do detailed solution studies to be confident of that mechanism. Our studies used

stirred solutions, which may promote solution nucleation in contrast to unstirred solutions.

Relevance to Biomineralization. A nucleation mechanism involving solution-formed nuclei which are adsorbed or transported to growth sites may also be relevant to biomineralization. Nuclei may be preformed in encapsulated environments where nucleation can be carefully controlled and limited and then delivered to bone growth sites. Precipitates of calcium phosphate have been found within matrix vesicles associated with the mineralization front of woven bone and cartilage.⁶ Ruptured vesicles have been observed at bone growth sites, implying that the vesicle-derived calcium phosphate is involved in bone growth.⁷⁴ Calcium phosphate may be nucleated in the presence of noncollagenous proteins such as BSP and transported to bone growth sites. The platelike morphology of the in vitro film shown in Figure 4 appears very similar to in vivo "cement lines" formed on top of resorbed bone in the presence of noncollagenous proteins but in the absence of collagen.⁷⁵

Conclusions

The nucleation and growth of calcium phosphate onto self-assembled monolayers from physiological-type solutions occurred by the adsorption of solution-formed crystallites, an alternative mechanism to heterogeneous nucleation onto surfaces. This work suggests that one way to grow apatite onto substrates is to promote the formation of nuclei in solution and then "trap" the growing crystallites onto surfaces by adsorption.

Nucleation in solution occurred after a long induction period and was evidenced by significant decreases in calcium and phosphorus ion concentrations. The induction time for solution nucleation increased with decreasing solution supersaturation. The solution nuclei started to grow, adsorbed onto the surfaces, and then grew until they coalesced to form dense apatite films, and then the crystallites grew vertically. The crystallites had platelike substructures and a degree of (002) orientation.

Future work is necessary to understand the mechanisms of growth of the solution-formed crystallites, the possibility of OCP precursors, and reasons for the high degree of orientation. In addition to elucidating a novel mechanism for calcium phosphate nucleation and growth, this work has importance for the formation of calcium phosphate films and nanostructures for bioactive implant coatings and biomolecular devices.

Acknowledgment. This research was supported by the U.S. Department of Energy (B.J.T.) and Pacific Northwest National Laboratory (PNNL) (C.C.C.). We gratefully acknowledge M. J. Van Stipdonk, D. R. Justes, and E. A. Schweikert at Texas A&M for development of the TOF-SIMS technique involving (CsI)Cs⁺ projectiles and use of their instrument and C. R. Samples and R. D. English for their technical assistance with it. We thank A. A. Campbell and P. C. Rieke for helpful discussions concerning calcium phosphate nucleation and use of a speciation calculation program. We are appreciative of technical assistance from M. Engelhard (XPS), J. Young (FEM), and D. McCready (XRD) at PNNL. A portion of the research described in this paper was performed in the Environmental Molecular Sciences Laboratory, a national scientific user facility sponsored by the Department of Energy's Office of Biological and Environmental Research and located at Pacific Northwest National Laboratory.

References and Notes

(1) Lowenstam, H. A.; Weiner, S. *On Biomineralization*; Oxford University Press: New York, 1989.

- (2) Shoen, F. J. H.; Kim, K. H.; Anderson, H. C.; Levy, R. J. *J. Biomed. Mater. Res. Appl. Biomater.* **1988**, *22*, 11–36.
- (3) Glimcher, M. J. In *Handbook of Physiology-Endocrinology*; Astwood, E. B., Ed.; Williams & Wilkins: Baltimore, 1976.
- (4) Hunter, G. K. In *Bone Metabolism and Mineralization*; Hall, B. K., Ed.; CRC Press: Boca Raton, FL, 1992; pp 225–247.
- (5) Roach, H. I. *Cell Biol. Int.* **1994**, *18*, 617–628.
- (6) Anderson, H. C. *Bone and Mineral Research*; Excerpta Medica: Amsterdam, 1985; Vol. 109.
- (7) Fisher, L. W.; Whitson, S. W.; Avioli, L. V.; Termine, J. D. *J. Biol. Chem.* **1983**, *248*, 12723–12727.
- (8) Shapiro, H. S.; Chen, J.; Wrona, J. L.; Zhang, Q.; Blum, M.; Sodek, J. *Matrix* **1993**, *13*, 431–441.
- (9) Termine, J. D.; Kleinman, H. K.; Whitson, S. W.; Conn, K. M.; McGarvey, M. L.; Martin, G. R. *Cell* **1981**, *26*, 99–105.
- (10) Franzen, A.; Heinegard, D. *Biochem. J.* **1985**, *232*, 715–724.
- (11) Gorski, J. P.; Simizu, K. *J. Biol. Chem.* **1988**, *263*, 15938–15945.
- (12) Chen, Y.; Bal, B. S.; Gorski, J. P. *J. Biol. Chem.* **1992**, *267*, 24871–24878.
- (13) Nancollas, G. H.; Tsortos, A.; Zeiba, A. *Scanning Microsc.* **1996**, *10*, 499–508.
- (14) Hirsch, D.; Azoury, R.; Sarig, S. *J. Cryst. Growth* **1990**, *104*, 759–765.
- (15) Kokubo, T.; Ito, S.; Huang, Z. T.; Hayashi, T.; Sakka, S. *J. Biomed. Mater. Res.* **1990**, *24*, 331–343.
- (16) Kokubo, T.; Hata, K.; Nakamura, T.; Yamamuro, T. *Bioceramics* **1991**, *4*, 113–120.
- (17) Tanahashi, M.; Kokubo, T.; Matsuda, T. *J. Biomed. Mater. Res.* **1996**, *31*, 243–249.
- (18) Tretinnikov, O. N.; Kato, K.; Ikada, Y. *J. Biomed. Mater. Res.* **1994**, *28*, 1365–1373.
- (19) Pereria, M. M.; Clark, A. E.; Hench, L. L. *J. Biomed. Mater. Res.* **1994**, *28*, 693–698.
- (20) Reis, R. L.; Cunha, A. M.; Fernandes, M. H.; Correia, R. N. *J. Mater. Sci.: Mater. Med.* **1997**, *8*, 897–905.
- (21) Kokubo, T. *Acta Mater.* **1998**, *46*, 2519–2527.
- (22) Kim, H. M.; Kim, Y.; Park, S. J.; Rey, C.; Lee, H. M.; Glimcher, M. J.; Ko, J. S. *Biomaterials* **2000**, *21*, 1129–1134.
- (23) Wu, W.; Nancollas, G. H. *Langmuir* **1997**, *13*, 861–865.
- (24) Koutsoukos, P. G.; Nancollas, G. H. *Colloids Surf.* **1987**, *28*, 95–108.
- (25) Dalas, E.; Kallitsis, J. K.; Koutsoukos, P. G. *Langmuir* **1991**, *7*, 1822–1826.
- (26) Spanos, N.; Koutsoukos, P. G. *J. Mater. Sci.* **2001**, *36*, 573–578.
- (27) Wu, W.; Nancollas, G. H. *J. Colloid Interface Sci.* **1998**, *199*, 206–211.
- (28) Dalas, E.; Ioannou, P. V.; Koutsoukos, P. *Langmuir* **1989**, *5*, 157–160.
- (29) Tanahashi, M.; Matsuda, T. *J. Biomed. Mater. Res.* **1997**, *34*, 305–315.
- (30) Mao, C.; Li, H.; Cui, F.; Feng, Q.; Wang, H.; Ma, C. *J. Mater. Chem.* **1998**, *8*, 2795–2801.
- (31) Mao, C. B.; Li, H. D.; Cui, F. Z.; Feng, Q. L.; Ma, C. L. *J. Mater. Chem.* **1999**, *9*, 2573–2582.
- (32) Bain, C. D.; Evall, J.; Whitesides, G. M. *J. Am. Chem. Soc.* **1989**, *111*, 7155–7164.
- (33) Finklea, H. O. In *Electroanalytical Chemistry—A Series of Advances*; Bard, A. J., Rubinstein, I., Eds.; Marcel Dekker: New York, 1996; Vol. 19.
- (34) Nuzzo, R. G.; Dubois, L. H.; Allara, D. L. *J. Am. Chem. Soc.* **1990**, *112*, 558–569.
- (35) Bunker, B. C.; Rieke, P. C.; Tarasevich, B. J.; Campbell, A. A.; Fryxell, G. E.; Graff, G. L.; Song, L.; Liu, J. *Science* **1994**, *264*, 48.
- (36) Tarasevich, B. J.; Rieke, P. C.; Liu, J. *J. Chem. Mater.* **1996**, *8*, 292–300.
- (37) Aisenberg, J.; Black, A. J.; Whitesides, G. M. *Nature* **1999**, *398*, 495–498.
- (38) Aizenberg, J.; Black, A. J.; Whitesides, G. M. *J. Am. Chem. Soc.* **1999**, *121*.
- (39) Numura, T.; Minemura, A. *Nippon Kagaku Kaishi* **1980**, 1621.
- (40) Schumacher, R. *Angew. Chem., Int. Ed. Engl.* **1990**, *29*, 329–343.
- (41) Ward, M. D.; Buttry, D. A. *Science* **1990**, *249*, 1000–1007.
- (42) Bain, C. D.; Troughton, E. B.; Tao, Y.-T.; Evall, J.; Whitesides, G. M.; Nuzzo, R. G. *J. Am. Chem. Soc.* **1989**, *111*, 321–335.
- (43) Parikh, A. N.; Allara, D. L. *J. Chem. Phys.* **1992**, *96*, 927–945.
- (44) Atre, S. V.; Liedberg, B.; Allara, D. L. *Langmuir* **1995**, *11*, 3882–3893.
- (45) Koutsoukos, P. G. Kinetics of Precipitation of Hydroxyapatite from Aqueous Solutions. Ph.D. Thesis, State University of New York at Buffalo, 1980.
- (46) McDowell, H.; Gregory, T. M.; Brown, W. E. *J. Res. Natl. Bur. Stand. (U.S.)* **1977**, *81A*, 273.

- (47) Gregory, T. M.; Moreno, E. C.; Patel, J. M.; Brown, W. E. *J. Res. Natl. Bur. Stand. (U.S.)* **1974**, 78A, 667.
- (48) Marshall, R. Ph.D. Thesis, State University of New York at Buffalo, 1970.
- (49) Kanazawa, K. K.; Gordon, J. G. *Anal. Chem.* **1985**, 57, 1770–1771.
- (50) Sauerbrey, G. Z. *Phys.* **1959**, 155, 206–222.
- (51) Martin, S. J.; Granstaff, V. E.; Frye, G. C. *Anal. Chem.* **1991**, 63, 221.
- (52) We observed a 10% error in atomic percents determined using Ca 2p compared to Ca 2s using manufacturer-determined sensitivity factors of 1.927 and 0.548, respectively, on thicker films that had no significant gold peaks. We attribute this to errors in the Ca 2s sensitivity factor. To correct for this in the determination of Ca/P ratios, Ca/P ratios determined using Ca 2s (Ca 2s/P) were corrected by a factor equivalent to Ca 2p/P divided by Ca 2s/P determined on thick standard films.
- (53) Kanzaki, N.; Onuma, K.; Ito, A.; Teraoka, K.; Tateishi, T.; Tsutsumi, S. *J. Phys. Chem. B* **1998**, 102, 6471–6476.
- (54) Chusuei, C. C.; Goodman, D. W.; Van Stipdonk, M. J.; Justes, D. R.; Schweikert, E. A. *Anal. Chem.* **1999**, 71, 149–153.
- (55) Ferrell, W. R.; von Heimburg, S. L.; Van Stipdonk, M. J.; Schweikert, E. A. *Int. J. Mass. Spectrom. Ion Processes* **1996**, 155, 89–97.
- (56) Chusuei, C. C.; Goodman, D. W.; Van Stipdonk, M. J.; Justes, D. R.; Lok, K. H.; Schweikert, E. A. *Langmuir* **1999**, 15, 7355–7360.
- (57) Tarasevich, B. J.; Chusuei, C. C.; Allara, D. L. Submitted for publication.
- (58) Lu, H. B.; Campbell, C. T.; Graham, D. J.; Ratner, B. D. *Anal. Chem.* **2000**, 72, 2886–2894.
- (59) Grabar, K. C.; Brown, K. R.; Keating, C. D.; Stranick, S. J.; Tang, S.-L.; Natan, M. *Anal. Chem.* **1997**, 69, 471–477.
- (60) Onuma, K.; Ito, A. *Chem. Mater.* **1998**, 10, 3346–3351.
- (61) Song, L.; Campbell, A. A.; Li, X. S.; Bunker, B. C. *Mater. Res. Soc. Symp. Proc.* **1996**, 414, 35–41.
- (62) Onuma, K.; Kanzaki, N.; Ito, A.; Tateishi, T. *J. Phys. Chem. B* **1998**, 102, 7833–7838.
- (63) Onuma, K.; Oyane, A.; Tsutsui, K.; Tanaka, K.; Treboux, G.; Kanzaki, N.; Ito, A. *J. Phys. Chem. B* **2000**, 104, 10563–10568.
- (64) Iijima, M.; Kamemizu, H.; Wakamatsu, N.; Goto, T.; Doi, Y.; Moriwaki, Y. *J. Cryst. Growth* **1997**, 181, 70–78.
- (65) Kapelos, J.; Koutsoukos, P. G. *Langmuir* **1999**, 15, 6557–6562.
- (66) Tarasevich, B. J.; Allara, D. L. Manuscript in preparation.
- (67) Belcher, A. M.; Wu, X. H.; Christensen, R. J.; Hansma, P. K.; Stucky, G. D.; Morse, D. E. *Nature* **1996**, 381, 56–58.
- (68) Tanahasi, M.; Yao, T.; Kokubo, T.; Minoda, M.; Miyamoto, T.; Nakamura, T.; Yamamuro, T. *J. Ceram. Soc. Jpn., Int. Ed.* **1994**, 102, 823–830.
- (69) Abe, Y.; Kokubo, T.; Yamamuro, T. *J. Mater. Sci.: Mater. Med. I* **1990**, 223–238.
- (70) Rhee, S.-H.; Tanaka, J. *Biomaterials* **1999**, 20, 2155–2160.
- (71) Hayakawa, S.; Tsuru, K.; Ohtsuki, C.; Osaka, A. *J. Am. Ceram. Soc.* **1999**, 82, 2155–2160.
- (72) Hata, K.; Kokubo, T.; Nakamura, T.; Yamamuro, T. *J. Am. Ceram. Soc.* **1995**, 78, 1049–1053.
- (73) Jokinen, M.; Peltola, T.; Simola, J.; Korventausta, J.; Yli-Urpo, A. In *Bioceramics*; Trans Tech Publications Ltd.: Zurich-Uetikon, Switzerland, 2000; Vol. 192-1, pp 601–604.
- (74) Boyan, B. D.; Schwartz, Z.; Swain, L. D.; Bonewald, L. F.; Khare, A. *Connect. Tissue Res.* **1989**, 22, 3–16.
- (75) Davies, J. E. *Anat. Rec.* **1996**, 245, 426–445.